IEEE Access
Multidisciplinary ⋮ Rapid Review ⋮ Open Access Journal

Received November 25, 2021, accepted December 16, 2021, date of publication December 23, 2021,
date of current version January 4, 2022.

Digital Object Identifier 10.1109/ACCESS.2021.3137641

Entry Guidance Command Generation for Hypersonic Glide Vehicles Under Threats and Multiple Constraints

ZIYAO WANG, SHENGJING TANG, AND JIE GUO

Key Laboratory of Dynamics and Control of Flight Vehicle, Ministry of Education, Beijing Institute of Technology, Beijing 100081, China
School of Aerospace Engineering, Beijing Institute of Technology, Beijing 100081, China

Corresponding author: Jie Guo (guojie1981@bit.edu.cn)

This work was supported in part by the National Natural Science Foundation of China under Grant 11202024 and Grant 11572036.

ABSTRACT A novel entry guidance command generation (EGCG) method for hypersonic glide vehicles (HGVs) is proposed in this paper. Apart from the conventional path constraints, terminal constraints, and multiple stationary geographic constraints, the method takes into account several threats that HGVs must avoid during the entry process. The threats are classified into covert threats and dynamic threats. The information of covert threats needs to be detected during the entry process, and the positions of dynamic threats are even unfixed. A piecewise analytical polynomial height-velocity profile is used to derive an analytical magnitude expression for bank angle commands. The profile is capable of taking full advantage of the width of the entry corridor and satisfying large range requirements in flight missions. An improved artificial potential field (IAPF) is introduced to formulate the lateral guidance law, which allows the HGV to pass all the waypoints, circumvent no-fly zones, and maneuver to avoid threats. Finally, several simulations are conducted to demonstrate the effectiveness of the designed method. The proposed EGCG method exhibits a superior ability to satisfy multiple constraints and avoid threats, accuracy to target point arrival, and strong robustness against uncertainties and deviations.

INDEX TERMS Hypersonic glide vehicle, entry guidance command generation, multiple constraints, threats, improved artificial potential field.

I. INTRODUCTION

The hypersonic glide vehicle (HGV), a current focal point in the research of aerospace engineering, is delivered to the scheduled altitude by a launch vehicle, and then enters the atmosphere without thrust [1], [2]. The dynamic system of HGVs is highly nonlinear, coupled, and uncertain due to the special and complex flight conditions, such as the nonlinear aerodynamics, high speed, high temperature, and extreme flight altitude, which make the trajectory planning and entry guidance of HGVs very challenging [3].

To nudge the HGV throughout flight toward the specified terminal point with strict constraints, the entry guidance command generation (EGCG) is required to be accurate and rapid. There are mainly three kinds of guidance strategies in the entry glide phase [4]. The first one is the predictor-corrector guidance method [5]–[8], which predicts the terminal states by conducting online trajectory simulations, and then corrects the guidance commands according to the deviations between the predicted and desired terminal states. The second method is online/offline trajectory optimization. Gauss pseudospectral method [9], particle swarm optimization method [10], [11], pigeon inspired optimization method [12], and convex optimization method [13], [14] are applied in the field of entry trajectory optimization. While the guidance methods mentioned above require an extremely large amount of calculation and thus pose a high requirement on the onboard computer, which is not conducive to engineering implementation. Conversely, profile-following guidance, the last kind of guidance strategies, needs less computationally expenditure and is easier to be implemented in practical engineering applications. The widely used profiles for the longitudinal trajectory planning of an HGV are drag-versus-velocity (D-V) profile [15], lift/drag-versus-energy (L/D-E) profile [16], [17], and drag-versus-energy (D-E) profile [1], [18]. A feasible D-E profile is generated in

The associate editor coordinating the review of this manuscript and approving it for publication was Xiwang Dong.

Reference [18] through interpolations between the upper and lower boundaries of the entry corridor to achieve the desired range. While the dynamic equations of an HGV need to be transferred with the energy first, which increases the complexity of the algorithm. The altitude-versus-velocity (h-V) profile can also be used for entry trajectory planning. The h-V profile is more direct to program the states h and V simultaneously for the EGCG, and the terminal guidance accuracy is more convenient to be guaranteed. In Reference [2], an entry trajectory based on a piecewise polynomial is designed in the h-V profile. While the main part of this h-V profile is straight but the entry corridor is bent due to the multiple path constraints, preventing the h-V profile from making full use of the width of the entry corridor. The range that the HGV can reach is highly dependent on the position of the h-V profile in the entry corridor. If the h-V profile is closer to the upper boundary of the entry corridor, the HGV can enter at a higher altitude with less drag and thus reach a larger range, and vice versa. Hence, fully utilizing the width of the entry corridor can increase the range of the HGV, whereas the method described in Reference [2] has a range limitation.

Moreover, the HGV has an excellent aerodynamic characteristic and a strong lateral maneuvering ability. Therefore, the HGV has the potential to cope with more complicated missions, such as avoidance of no-fly zones and multi-waypoints delivery. Designing a heading error corridor-based bank angle reversal logic is an effective way to satisfy geographic constraints. The artificial potential field (APF) method is one of the most popular algorithms in obstacle avoidance for mobile robots [19], unmanned aerial vehicles (UAVs) [20], autonomous vehicles [21], [22], and manipulators [23], which has the benefits of brief mathematical description, simplicity, high efficiency, and strong adaptability. But the local minimum problem is a drawback of the APF method that should be noticed. When the APF method is applied to the trajectory planning of low-speed vehicles, the vehicles may become trapped in the local minimum point of the APF. However, the HGV does not have this issue. Due to the HGV's high velocity, when it reaches the local minimum point, it will automatically rush out and continue flying forward. In Reference [24], the APF method is applied in the bank angle reversal logic of an HGV to reduce terminal heading error and to avoid no-fly zones. Reference [25] proposed a lateral entry guidance algorithm based on the APF method for waypoint passage and no-fly zones avoidance. Reference [26] combined the APF method with the threat quantitative evaluation to realize complex distributed no-fly zone avoidance. By and large, these guidance methods could be effectively applied in the entry guidance to meet the conventional geographic constraints.

However, none of these approaches examine the covert threats detected during the entry process nor take the dynamic threats into account. During the entry process, reconnaissance satellites or early warning radars may detect new enemy concealed defensive positions, which are covert threats. The vehicle also needs to avoid detection by enemy airborne warning systems and attack by interceptors, which are dynamic threats. The two kinds of threats have not been considered in the current study about entry guidance algorithms. These threats require the HGV to possess a strong online guidance capability. Hence, a novel lateral guidance law based on an improved artificial potential field (IAPF) mothed is proposed to meet these demands in this paper.

The highlights of this paper are mainly summarized as follows.

1. Besides the conventional path constraints, terminal constraints, and multiple stationary geographic constraints, threats containing immobile covert threats and unfixed dynamic threats are considered as new constraints in the process of entry guidance.

2. An analytical magnitude expression of bank angle commands is derived from a new piecewise analytical polynomial h-V profile, which makes the HGV capable to be robust against aerodynamic uncertainties and initial state deviations. The h-V profile is determined by the upper and lower boundaries of the entry corridor, which is beneficial to fully use the width of the entry corridor and reach a large range.

3. Different IAPFs are established on the characteristics of waypoints, no-fly zones, and threats, respectively. A novel lateral guidance logic is designed based on the IAPF method.

The rest of the paper is organized as follows. Section II presents the dynamic equations of the vehicle and multiple trajectory constraints, as well as the mathematical expression of threats. Section III develops a new longitudinal entry trajectory in the h-V profile and generates the analytical magnitude expression of bank angle guidance commands. Section IV introduces the IAPF mothed and designs a lateral guidance law that satisfies geographic constraints and considers threats. In Section V, the effectiveness of the proposed guidance scheme is demonstrated by simulating different entry scenarios of the CAV-H model. Concluding remarks are drawn in Section VI.

II. PRELIMINARIES

The necessary backgrounds, including the entry dynamic equations, multiple trajectory constraints, and threats detected during the entry process, for HGVs are described in this section.

A. PENTRY DYNAMIC EQUATIONS

As shown in Fig. 1, the movement of the HGV from the Geocentric Equatorial Rotating frame $E-x_{\mathrm{e}}y_{\mathrm{e}}z_{\mathrm{e}}$ is illustrated and the local North-East-Down frame $o-xyz$ is utilized to clarify the HGV's states [1].

Regarding the HGV as a particle, the three-degree-of-freedom equations of motion are used to represent an HGV gliding over a spherical, rotating Earth, which are as follows.

$$\dot{r} = V\sin\theta \tag{1}$$

$$\dot{\lambda} = \frac{V\cos\theta\sin\psi}{r\cos\phi} \tag{2}$$

$$\dot{\phi} = \frac{V\cos\theta\cos\psi}{r} \tag{3}$$

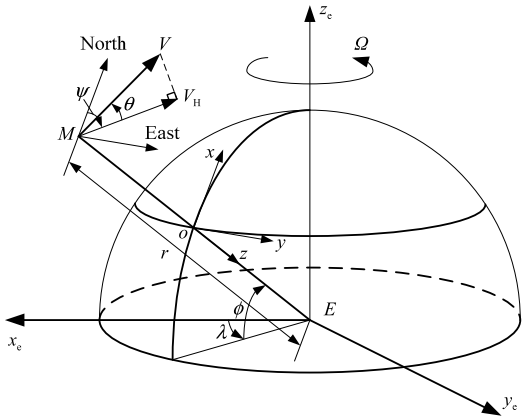

FIGURE 1. The GER frame and NED frames.

$$\dot{V} = -D - g\sin\theta + \Omega^2 r\cos\phi \times (\sin\theta\cos\phi - \cos\theta\sin\phi\cos\psi) \quad (4)$$

$$\dot{\theta} = \frac{L\cos\sigma}{V} + \left(\frac{V}{r} - \frac{g}{V}\right)\cos\theta + 2\Omega\cos\phi\sin\psi + \frac{\Omega^2 r}{V}\cos\phi\,(\cos\theta\cos\phi + \sin\theta\sin\phi\cos\psi) \quad (5)$$

$$\dot{\psi} = \frac{L\sin\sigma}{V\cos\theta} + \frac{V}{r}\cos\theta\sin\psi\tan\phi + \frac{\Omega^2 r}{V\cos\theta} \times \sin\psi\sin\phi\cos\phi - 2\Omega\,(\tan\theta\cos\phi\cos\psi - \sin\phi) \quad (6)$$

where r is the radius from the Earth center to the vehicle; λ and ϕ are the longitude and latitude, respectively; V is the Earth-relative velocity of the HGV, and V_H is the horizontal projection of V shown in Fig. 1; θ is the flight path angle, which is the angle between V and V_H; ψ is the heading angle measured from the north in the clockwise direction. σ is the bank angle. Ω is the rotational angular velocity of the Earth, and g is the gravitational acceleration, which is obtained by $g = g_0 R_e^2/r^2$, where g_0 is the gravitational acceleration at sea level, and R_e is the radius of the Earth. L and D are the lift and drag accelerations, respectively, which can be calculated by

$$L = \frac{1}{2m}\rho V^2 C_L(\alpha, Ma) S_{ref} \quad (7)$$

$$D = \frac{1}{2m}\rho V^2 C_D(\alpha, Ma) S_{ref} \quad (8)$$

where m is the mass of the HGV; C_L and C_D are the lift and drag coefficients, respectively; α is the angle of attack (AOA); Ma is the Mach number of the HGV; S_{ref} is the reference area of the HGV; ρ is the atmosphere density, whose expression is

$$\rho(h) = \rho_0 e^{-h/h_s} \quad (9)$$

where $h = r - R_e$ is the altitude of the HGV, $\rho_0 = 1.225\,\mathrm{kg/m^3}$ is the atmospheric density at sea level, and $h_s = 6700\,\mathrm{m}$.

B. TRAJECTORY CONSTRAINTS

1) PATH CONSTRAINTS

For flight safety, the entry trajectory should satisfy the constraints on the stagnation point heating rate $\dot{Q}$, the dynamic pressure q, and the total aerodynamic load n, as follows.

$$\dot{Q} = k_Q \rho^{0.5} V^{3.15} \le \dot{Q}_{max} \quad (10)$$

$$q = \frac{1}{2}\rho V^2 \le q_{max} \quad (11)$$

$$n = \frac{\sqrt{L^2 + D^2}}{g} \le n_{max} \quad (12)$$

where $\dot{Q}_{max}$, q_{max}, n_{max} are the maximum allowable heating rate, the maximum dynamic pressure, and the maximum total aerodynamic load, respectively; $k_Q = 7.97 \times 10^{-8}$ is a heat transfer coefficient. These three constraints are rigid constraints, which must be satisfied.

Besides, the quasi-equilibrium glide condition (QEGC) is introduced as a soft constraint to attenuate the altitude phugoid oscillation along the entry trajectory. The flight path angle is small and varies relatively slow in a major portion of a lifting entry trajectory [27]. Hence, setting $\theta = 0$ and $\dot{\theta} = 0$ in Eq. (5) and ignoring the Earth rotation produces

$$\frac{L\cos\sigma}{V} + \left(\frac{V}{r} - \frac{g}{V}\right) = 0 \quad (13)$$

Since $\cos\sigma \le 1$ must be satisfied, we obtain

$$L + \left(\frac{V^2}{r} - g\right) \ge 0 \quad (14)$$

which is called the QEGC. It means that the bank angle is capable of controlling the flight path angle as long as h-V profile is located below the QEGC boundary.

2) TERMINAL CONSTRAINTS

Different flight missions correspond to different terminal conditions. In this paper, terminal constraints are considered as the terminal target point P_f^* whose position coordinate is (λ_f^*, ϕ_f^*), the specified final altitude h_f^*, velocity V_f^*, flight path angle θ_f^*, as well as the ultimate heading error $\delta\psi_f$, which are given as follows.

$$\begin{cases} \Delta h_f = |h_f - h_f^*| \le \delta h_f, & \Delta\lambda_f = |\lambda_f - \lambda_f^*| \le \delta\lambda_f \\ \Delta\phi_f = |\phi_f - \phi_f^*| \le \delta\phi_f, & \Delta V_f = |V_f - V_f^*| \le \delta V_f \\ \Delta\theta_f = |\theta_f - \theta_f^*| \le \delta\theta_f, & \Delta\psi_f = |\psi_f - \psi_{LOS}| \le \delta\psi_f \end{cases} \quad (15)$$

where Δh_f, $\Delta\lambda_f$, $\Delta\phi_f$, ΔV_f, and $\Delta\theta_f$ are the terminal state errors meaning the deviations between the terminal states h_f, λ_f, ϕ_f, V_f, and θ_f at the terminal time t_f and the specified final states, $\Delta\psi_f$ is the heading error defined as the deviation between the terminal heading angle ψ_f and the line-of-sight (LOS) angle ψ_{LOS} towards the target, δh_f, $\delta\lambda_f$, $\delta\phi_f$, δV_f, $\delta\theta_f$, $\delta\psi_f$, and δs_f are the tolerance deviations of corresponding states, respectively.

3) MULTIPLE GEOGRAPHIC CONSTRAINTS

Similar to existing research, stationary waypoints and no-fly zones are considered in this paper.

Waypoints are specified as intermediate coordinates to fly over before reaching the terminal target to satisfy payload deliveries or reconnaissance mission requirements [9], [25]. However, the time, altitude, velocity, flight path angle, control variables, and heading angle for waypoint passage are not constrained. Since there may be multiple waypoints, with a total of L, assuming $P_{\mathrm{W}i}\,(i = 1, 2, \ldots, L)$ is a waypoint and $(\lambda_{\mathrm{W}i}, \phi_{\mathrm{W}i})$ is the corresponding coordinate, the waypoints are ordered by the distances to the entry point, which can be expressed as

$$s\left(P_0, P_{\mathrm{W}1}\right) \leq s\left(P_0, P_{\mathrm{W}2}\right) \leq \cdots \leq s\left(P_0, P_{\mathrm{W}L}\right) \tag{16}$$

where $P_0 = (\lambda_0, \phi_0)^{\mathrm{T}}$ is the coordinate of the initial entry point, s is the great arc distance, which can be calculated by

$$\begin{aligned} &s\left[P_1\left(\lambda_1, \phi_1\right), P_2\left(\lambda_2, \phi_2\right)\right] \\ &\quad = R\cos^{-1}\left[\cos\phi_1\cos\phi_2\cos\left(\lambda_1 - \lambda_2\right) + \sin\phi_1\sin\phi_2\right] \end{aligned} \tag{17}$$

Thus, the constraint for $P_{\mathrm{W}i}$ is expressed as

$$\left|\tilde{\lambda} - \lambda_{\mathrm{W}i}\right| \leq \varepsilon_\lambda, \left|\tilde{\phi} - \phi_{\mathrm{W}i}\right| \leq \varepsilon_\phi \tag{18}$$

where $\left(\tilde{\lambda}, \tilde{\phi}\right)$ is the point on entry trajectory subjects to the condition $P\left(\tilde{\lambda}, \tilde{\phi}\right) = \arg\min_P s\left[P\left(\lambda, \phi\right), P_{\mathrm{W}i}\left(\lambda_{\mathrm{W}i}, \phi_{\mathrm{W}i}\right)\right]$, and ε_λ, ε_ϕ are small preselected positive values.

In contrast, a no-fly zone is a region with a boundary that the HGV may contact but must not violate [9]. The no-fly zones include stationary threat avoidance or geopolitical restrictions, which are preset before launch [25]. The no-fly zone model is an infinitely high cylinder, whose center is $P_{\mathrm{N}j}\,(j = 1, 2, \ldots, M)$ with a radius of $R_{\mathrm{N}j}$, and the coordinate of the center is $\left(\lambda_{\mathrm{N}j}, \phi_{\mathrm{N}j}\right)$, which is constant. Similar to the order of the waypoints, the no-fly zones are arranged in order of the distances to the entry point, which is

$$s\left(P_0, P_{\mathrm{N}1}\right) \leq s\left(P_0, P_{\mathrm{N}2}\right) \leq \cdots \leq s\left(P_0, P_{\mathrm{N}M}\right) \tag{19}$$

Thus, the constraint of no-fly zones is expressed in the following form.

$$s\left[P\left(\lambda, \phi\right), P_{\mathrm{N}j}\left(\lambda_{\mathrm{N}j}, \phi_{\mathrm{N}j}\right)\right] \geq R_{\mathrm{N}j} \quad (j = 1, 2, \ldots, M) \tag{20}$$

C. THREATS DURING THE ENTRY PROCESS

Different from existing research, the paper takes into consideration the influence of threats during the entry process. All the information of constraints mentioned above is preset before launch and remains unchanged during the entry process. On the contrary, the intelligence of threats is unknown before launch. The position and motion information of threats need to be detected by reconnaissance satellites or airborne radars during the entry process. This is rational because reconnaissance satellites or airborne radars can provide accurate and timely information about threats in practice. Reconnaissance satellites have a centimeter-level accuracy. The broad range of reconnaissance capabilities can assist the HGV in detecting threats along the entry trajectory. Because threat information only contains the coordinate and the threat range, the data link technology enables the reconnaissance satellite to transmit the information to the HGV accurately and rapidly. The accuracy of the airborne radars is slightly greater, up to a few tens of meters, which also meets the detect demand. The threats contain two kinds:

1. Covert threats. Reconnaissance satellites or airborne radars have a limited range of detection, so some covert missile defense systems can only be detected when the HGV approaches them. The location of covert threats is immobile.

2. Dynamic threats. The HGV needs to elude the detection of airborne early warning aircraft and the attack of interceptors. The position of dynamic threats changes real-timely during the entry process.

The HGV needs to keep a safe distance from these threats. For simplification, all the threats are considered as infinitely high cylinders, regardless of the height of threats. The position of a threat is assumed as $P_{\mathrm{T}k}\,(k = 1, 2, \ldots, N)$, whose coordinate is $\left(\lambda_{\mathrm{T}k}\left(t\right), \phi_{\mathrm{T}k}\left(t\right)\right)$, maybe changing with time. The minimum safe distance that the HGV should keep is $R_{\mathrm{T}k}$. Only when the threat gets into the detection range R_{det} of reconnaissance satellites or airborne radars, the HGV detects the threat and acquires the information. Thus the constraint of threats is expressed as follows.

$$\begin{aligned} &\text{if } s\left[P\left(\lambda, \phi\right), P_{\mathrm{T}k}\left(\lambda_{\mathrm{T}k}\left(t\right), \phi_{\mathrm{T}k}\left(t\right)\right)\right] \leq R_{\mathrm{det}}, \\ &\qquad s\left[P\left(\lambda, \phi\right), P_{\mathrm{T}k}\left(\lambda_{\mathrm{T}k}\left(t\right), \phi_{\mathrm{T}k}\left(t\right)\right)\right] \geq R_{\mathrm{T}k} \\ &\qquad\qquad (k = 1, 2, \ldots, N) \end{aligned} \tag{21}$$

III. LONGITUDINAL GUIDANCE COMMAND GENERATION

The purpose of this paper is to design the proper guidance commands, the AOA α and the bank angle σ, to stably steer the HGV to the terminal target point with satisfying all the trajectory constraints and avoiding all the threats.

In this section, the scheme generates the longitudinal profile by taking into consideration the path and terminal constraints [28]. The h-V profile is utilized to design the entry corridor and determine the maximum and minimum boundaries allowed.

The entry trajectory is divided into two phases: the initial descent phase and the glide phase. In the initial descent phase, the flight altitude is too high, and the atmospheric density is insufficient to provide enough aerodynamic lift. So the QEGC is not valid, and the HGV rarely possesses lateral mobility in the initial descent phase. In the glide phase, the atmospheric density becomes relatively high and the lift is sufficient for lateral maneuver that could satisfy the multiple constraints. The interface between the two phases is named the transition point, which is demonstrated in Fig. 2 as $(V_{\mathrm{tran}}, h_{\mathrm{tran}})$.

Since the boundaries of the path constraints (10)-(12), and (14) are obtained under a certain AOA, it is necessary

to design a nominal AOA in advance. The boundaries of the entry corridor can be determined uniquely once the AOA α is specified.

As a consequence of the split flight phases, the AOA command is separated for each phase. At the beginning of the entry process, the HGV descents rapidly, so the baseline AOA is set to its maximum allowable value, which helps the HGV rise as soon as possible and minimizes the peak of the heating rate. Later in the stable glide phase, the HGV glides along with the AOA of the largest lift-to-drag ratio to achieve the best flight performance. The nominal AOA is defined as a function of velocity, which can be expressed as

$$\alpha = \begin{cases} \alpha_{\max} & \left(V > V_{\alpha_1}\right) \\ \dfrac{\alpha_{L/D_{\max}} - \alpha_{\max}}{V_{\alpha_2} - V_{\alpha_1}}\left(V - V_{\alpha_1}\right) + \alpha_{\max} & \left(V_{\alpha_2} \le V \le V_{\alpha_1}\right) \\ \alpha_{L/D_{\max}} & \left(V < V_{\alpha_2}\right) \end{cases} \tag{22}$$

where $\alpha_{\max}$ is the maximum of the AOA, $\alpha_{L/D_{\max}}$ is the AOA that has the largest lift-to-drag ratio, V_{α_1} and V_{α_2} are two specific velocities.

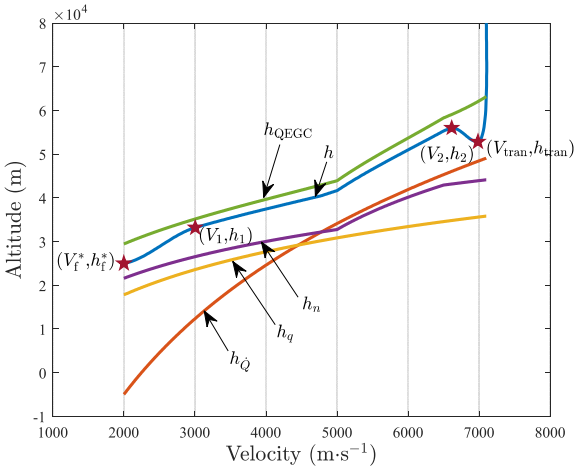

FIGURE 2. The entry corridor in the *h-V* profile.

Hence, the path constraints can be transformed into an entry corridor in the *h-V* profile, which is given by

$$h_{\max}(V) = h_{\mathrm{QEGC}}(V) \tag{23}$$

$$h_{\min}(V) = \max\left(h_{\dot{Q}}(V), h_q(V), h_n(V)\right) \tag{24}$$

where $h_{\max}(V)$ and $h_{\min}(V)$ are the upper and lower boundaries of the entry corridor, respectively. $h_{\mathrm{QEGC}}(V)$, $h_{\dot{Q}}(V)$, $h_q(V)$, and $h_n(V)$ represent the altitude constraints of QEGC, dynamic pressure, aerodynamic load, and heating rate under a certain velocity, respectively, which are depicted in Fig. 2.

A. INITIAL DESCENT PHASE

For the initial descent phase, under the frame of the nominal AOA, a constant bank angle σ_{ini} is introduced to generate a trajectory. The suitable value of σ_{ini} is chosen by starting from zero and increasing a magnitude by a small increment until a smooth transition condition and the path constraints are satisfied. The transition condition between the initial descent phase and the glide phase takes the form

$$\left|\frac{\mathrm{d}h}{\mathrm{d}V} - \left(\frac{\mathrm{d}h}{\mathrm{d}V}\right)_{\mathrm{QEGC}}\right| < \delta_{\mathrm{tran}} \tag{25}$$

where

$$\frac{\mathrm{d}h}{\mathrm{d}V} = -\frac{V\sin\theta}{D + g\sin\theta} \tag{26}$$

$(\mathrm{d}h/\mathrm{d}V)_{\mathrm{QEGC}}$ is the derivative of H concerning V along QEGC, and δ_{tran} is a small positive constant. The HGV enters the gliding phase after meeting the transition condition. The sign of σ is determined by the lateral guidance law based on the IAPF mothed, which is presented in Section IV-A1.

B. GLIDE PHASE

The glide phase is the crucial part of the entire entry process, which requires steering the HGV to glide smoothly and rigorously satisfying all path constraints and terminal constraints. The guidance command of σ in the glide phase contains two parts, i.e.

$$\cos\sigma = \cos\sigma_{\mathrm{ref}} + \Delta\sigma \tag{27}$$

where σ_{ref} is the reference command generated by the reference *h-V* profile, $\Delta\sigma$ is the tracking command to guarantee the HGV to track the reference *h-V* profile with the influence of the Earth rotation, aerodynamic uncertainties, and initial state deviations.

A piecewise analytical polynomial is chosen to design the reference *h-V* profile because the piecewise analytical polynomial has advantages for satisfying the multiple constraints encountered during the entry mission. The polynomial is divided into three phases. The first phase follows the initial descent phase. The purpose of the first phase is to ensure a smooth transition from the initial descent phase to the glide phase. The middle phase of the piecewise analytical polynomial is employed to satisfy the range constraint and ensure that the HGV reaches the terminal coordinate accurately. To make full use of the width of the entry corridor, the middle phase is designed mainly parallel to the boundaries of the entry corridor. The *h-V* profile can be as close to the upper boundary as possible and the HGV can reach a very large range. The last phase of the polynomial is intended to satisfy the terminal constraints. The expression of the *h-V* profile is as follows.

$$h_{\mathrm{ref}}(V) = \begin{cases} k_{23}V^3 + k_{22}V^2 + k_{21}V + k_{20} \\ \qquad V_2 \le V \le V_{\mathrm{tran}} \\ h_{\max}(V) - k\left(h_{\max}(V) - h_{\min}(V)\right) \\ \qquad V_1 \le V \le V_2 \\ k_{13}V^3 + k_{12}V^2 + k_{11}V + k_{10} \\ \qquad V_{\mathrm{f}}^* \le V \le V_1 \end{cases} \tag{28}$$

where h_{ref} is the reference altitude, k_{ij} $(i = 1, 2; j = 0, 1, 2, 3)$ are polynomial coefficients, V_1, V_2 are preselect velocities at two segment points, and k is the key proportionality coefficient determining the reference altitude and range of the HGV. The selection of segment points is not strict, but every phase should be long enough to provide a smooth transition. When k decreases, the glide trajectory in the reference h-V profile will be closer to the higher boundary, which increases the reference altitude and the range of the HGV.

For the continuity and the smoothness at the transition points $(V_{\text{tran}}, h_{\text{tran}})$ and (V_2, h_2), the first third-order polynomial in Eq. (28) can be determined by four constraints as follows.

$$\begin{cases} k_{23}V_{\text{tran}}^3 + k_{22}V_{\text{tran}}^2 + k_{21}V_{\text{tran}} + k_{20} = h_{\text{tran}} \\ k_{23}V_2^3 + k_{22}V_2^2 + k_{21}V_2 + k_{20} = h_2 \\ 3k_{23}V_{\text{tran}}^2 + 2k_{22}V_{\text{tran}} + k_{21} = \left(\mathrm{d}h_{\text{ref}}/\mathrm{d}V\right)_{\text{tran}} \\ 3k_{23}V_2^2 + 2k_{22}V_2 + k_{21} = \left(\mathrm{d}h_{\text{ref}}/\mathrm{d}V\right)_2 \end{cases} \tag{29}$$

where $\left(\mathrm{d}h_{\text{ref}}/\mathrm{d}V\right)_{\text{tran}}$ is the right-hand derivative at $(V_{\text{tran}}, h_{\text{tran}})$, and $\left(\mathrm{d}h_{\text{ref}}/\mathrm{d}V\right)_2$ is the left-hand derivative at (V_2, h_2).

Similarly, in consideration of the smooth connection at the transition point (V_1, h_1) and the satisfaction of the terminal constraints, the other third-order polynomial in Eq. (28) is calculated as follows.

$$\begin{cases} k_{13}V_1^3 + k_{12}V_1^2 + k_{11}V_1 + k_{10} = h_1 \\ k_{13}V_{\text{f}}^{*3} + k_{12}V_{\text{f}}^{*2} + k_{11}V_{\text{f}}^* + k_{10} = h_{\text{f}}^* \\ 3k_{13}V_1^2 + 2k_{12}V_1 + k_{11} = \left(\mathrm{d}h_{\text{ref}}/\mathrm{d}V\right)_1 \\ 3k_{13}V_{\text{f}}^{*2} + 2k_{12}V_{\text{f}}^* + k_{11} = \left(\mathrm{d}h_{\text{ref}}/\mathrm{d}V\right)_{\text{f}}^* \end{cases} \tag{30}$$

where $\left(\mathrm{d}h_{\text{ref}}/\mathrm{d}V\right)_1$ is the right-hand derivative at (V_1, h_1), and $\left(\mathrm{d}h_{\text{ref}}/\mathrm{d}V\right)_{\text{f}}^*$ can be calculated as follows.

$$\left(\frac{\mathrm{d}h_{\text{ref}}}{\mathrm{d}V}\right)_{\text{f}}^* = \frac{V_{\text{f}}^* \sin\theta_{\text{f}}^*}{-D_{\text{f}}^* - g_{\text{f}}^* \sin\theta_{\text{f}}^*} \tag{31}$$

where D_{f}^* and g_{f}^* are the drag acceleration and the gravitational acceleration at $\left(V_{\text{f}}^*, h_{\text{f}}^*\right)$.

So far the whole analytical reference h-V profile is established and demonstrated in Fig. 2, which is only determined by the coefficient k. The choice of k is based on the secant method about the terminal range error.

$$k^{(i+1)} = k^{(i)} - \frac{k^{(i)} - k^{(i-1)}}{\Delta s_{\text{f}}^{(i)} - \Delta s_{\text{f}}^{(i-1)}} \Delta s_{\text{f}}^{(i)} \tag{32}$$

where Δs_{f} is the terminal range error. To get the analytical expression of the magnitude of σ_{ref}, we can get the following formulae from Eq. (1), (4), and (5).

$$\frac{\mathrm{d}h_{\text{ref}}}{\mathrm{d}V} = \frac{V \sin\theta_{\text{ref}}}{-D - g\sin\theta_{\text{ref}}} \tag{33}$$

$$\frac{\mathrm{d}\theta_{\text{ref}}}{\mathrm{d}V} = \frac{L\cos\sigma + \left(V^2/r - g\right)\cos\theta_{\text{ref}}}{V\left(-D - g\sin\theta_{\text{ref}}\right)} \tag{34}$$

The rotation of the Earth is neglected in Eq. (33) and (34)because the tracking command $\Delta\sigma$ will compensate for the deviation caused by the Earth rotation. Then, the reference flight path angle θ_{ref} can be calculated as

$$\theta_{\text{ref}} = \arcsin\left[\frac{-D\left(\mathrm{d}h_{\text{ref}}/\mathrm{d}V\right)}{V + g\left(\mathrm{d}h_{\text{ref}}/\mathrm{d}V\right)}\right] \tag{35}$$

Hence, the partial derivative of θ_{ref} with respect to V is (36), as shown at the bottom of the next page.

Last, substitute the above equation into Eq. (34), and reference command σ_{ref} can be analytically expressed as follows (37), as shown at the bottom of the next page.

This formula is an analytical function of current states and thus computationally tractable.

The tracking command $\Delta\sigma$ is designed by the proportional-integral-derivative (PID) control as

$$\Delta\sigma = -k_{\text{P}}\left(h - h_{\text{ref}}\right) - k_{\text{I}} \times \int_{V_{\text{f}}}^{V_{\text{tran}}} \left(h - h_{\text{ref}}\right)\mathrm{d}V - k_{\text{D}}\mathrm{d}\left(h - h_{\text{ref}}\right)/\mathrm{d}V \tag{38}$$

where k_{P}, k_{I} and k_{D} are positive constants.

Considering the range of the bank angle, the magnitude of σ is determined as

$$|\sigma| = \begin{cases} 0 & \cos\sigma_{\text{ref}} + \Delta\sigma > 1 \\ \arccos\left(\cos\sigma_{\text{ref}} + \Delta\sigma\right) & 0 \le \cos\sigma_{\text{ref}} + \Delta\sigma \le 1 \\ \pi/2 & \cos\sigma_{\text{ref}} + \Delta\sigma < 0 \end{cases} \tag{39}$$

The sign of σ is determined by the lateral guidance law in Section IV.

IV. LATERAL GUIDANCE LAW DESIGN

A. IMPROVED ARTIFICIAL POTENTIAL FIELD DESIGN

Besides the simple mathematical description and strong adaptability, the APF method possesses the ability to offer smooth and feasible trajectories for avoiding no-fly zones in complex environments [20]. The basic thought of the APF method is to regard the motion space of the HGV as a virtual potential field. The terminal target point and waypoints generate attractive forces on the HGV, and on the contrary, the no-fly zones and threats provide repulsive forces. The HGV glides towards the terminal position under the combined action of attractive forces and repulsive forces. In this section, an IAPF is designed to satisfy the circumvention of no-fly zones and threats, and complete the flight mission about passing waypoints and reaching the terminal position with high fidelity. In comparison to the traditional APF, the IAPF proposed in this paper is enhanced by the use of several forms based on the features of waypoints, no-fly zones, and threats. The improved virtual attractive potential field is layered by waypoints to guarantee the HGV to pass through each one. Inspired by Reference [25], in addition to the virtual repulsive effect for avoiding no-fly zones and threats, the improved repulsive potential fields are designed with attraction to the next waypoint. The virtual forces of the HGV generated by the IAPF are shown in Fig. 3.

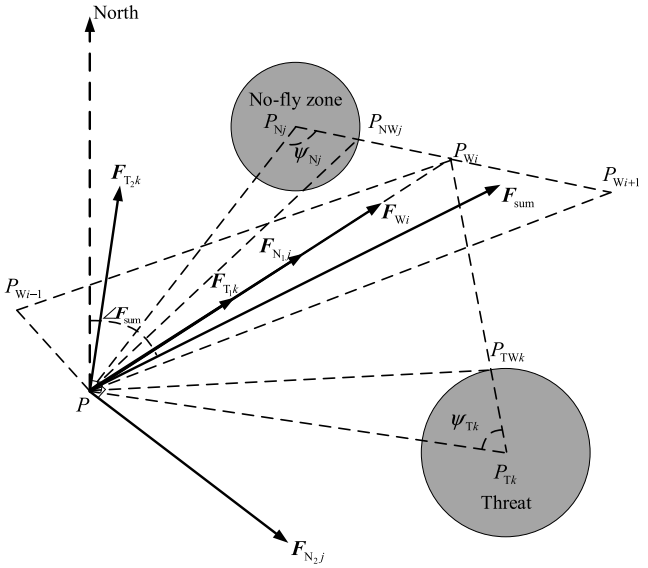

FIGURE 3. The virtual forces of the HGV.

1) THE IMPROVED VIRTUAL ATTRACTIVE POTENTIAL FIELD OF WAYPOINTS

In the purpose of guaranteeing the HGV to pass all the waypoints, when the HGV glides between the $(i-1)$th waypoint and the ith waypoint, the HGV is only attracted by the later waypoint. The terminal target point is regarded as another waypoint, i.e. the $(L+1)$th waypoint. Hence, the improved virtual attractive potential field is designed as follows.

$$U_{Wi}(P)=\begin{cases} k_W \ln\left[s\left(P,P_{Wi}\right)\right] \\ \quad \left(\angle PP_{Wi-1}P_{Wi}\le\dfrac{\pi}{2}<\angle PP_{Wi}P_{Wi+1}\right) \\ 0 \\ \quad \left(\angle PP_{Wi-1}P_{Wi}>\dfrac{\pi}{2}\ \text{or}\ \angle PP_{Wi}P_{Wi+1}\le\dfrac{\pi}{2}\right) \end{cases} \\ (i=1,2,\ldots,L,L+1) \tag{40}$$

where k_W is the attractive coefficient. The improved virtual attractive potential field of waypoints is shown in Fig. 4.

The improved virtual attractive force is the negative gradient of the improved attractive potential field, which can be calculated as

$$\boldsymbol{F}_{Wi}(P)=-\nabla U_{Wi}(P) =\begin{cases} \dfrac{k_W}{s\left(P,P_{Wi}\right)}\boldsymbol{n}_{Wi} \\ \quad \left(\angle PP_{Wi-1}P_{Wi}\le\dfrac{\pi}{2}<\angle PP_{Wi}P_{Wi+1}\right) \\ 0 \\ \quad \left(\angle PP_{Wi-1}P_{Wi}>\dfrac{\pi}{2}\ \text{or}\ \angle PP_{Wi}P_{Wi+1}\le\dfrac{\pi}{2}\right) \end{cases} \\ (i=1,2,\ldots,L,L+1) \tag{41}$$

The closer the HGV is to the waypoint, the larger the attractive force is. $\boldsymbol{n}_{Wi}=[\sin\psi_{Wi},\cos\psi_{Wi}]^T$ is the unit vector representing the direction from the HGV to the ith waypoint, and the ψ_{Wi} is the corresponding heading angle, and can be calculated as

$$\psi_{Wi}=\angle\boldsymbol{F}_{Wi}(\boldsymbol{p})=\psi_b\left(P,P_{Wi}\right) \tag{42}$$

where $\psi_b\left[P_1\left(\lambda_1,\phi_1\right),P_2\left(\lambda_2,\phi_2\right)\right]$ is the bearing at P_1 pointing to P_2, which is measured clockwise from the local north and is expressed as

$$\psi_b\left[P_1\left(\lambda_1,\phi_1\right),P_2\left(\lambda_2,\phi_2\right)\right] =\tan^{-1}\left[\frac{\sin\left(\lambda_2-\lambda_1\right)}{\cos\phi_1\tan\phi_2-\sin\phi\cos\left(\lambda_2-\lambda_1\right)}\right] \tag{43}$$

2) THE IMPROVED VIRTUAL REPULSIVE POTENTIAL FIELD OF NO-FLY ZONES

For the no-fly zones preset before launch, the improved virtual repulsive potential field is introduced by

$$U_{Nj}(P)=\begin{cases} \dfrac{1}{2}k_N\dfrac{s\left(P,P_{Wi}\right)^2 s\left(P,P_{Nj}\right)\psi_{Nj}}{\left[s\left(P,P_{Nj}\right)-R_{Nj}\right]^3} \\ \quad \left(s\left(P,P_{Nj}\right)\ge R_{Nj},\angle PP_{NWj}P_{Wi}>\dfrac{\pi}{2}\right) \\ 0 \\ \quad \left(s\left(P,P_{Nj}\right)\ge R_{Nj},\angle PP_{NWj}P_{Wi}\le\dfrac{\pi}{2}\right) \end{cases} \\ (j=1,2,\ldots,M) \tag{44}$$

where k_N is the repulsive coefficient of no-fly zones, $\psi_{Nj}=\angle PP_{Nj}P_{Wi}$ as shown in Fig. 3, P_{Wi} is the next waypoint that the HGV needs to pass, P_{NWj} is the intersection point between the edge of the jth no-fly zone and the connecting line of

$$\frac{\mathrm{d}\theta_{ref}}{\mathrm{d}V}=\frac{-D\left(\mathrm{d}^2h_{ref}/\mathrm{d}V^2\right)\left[V+g\left(\mathrm{d}h_{ref}/\mathrm{d}V\right)\right]+D\left(\mathrm{d}h_{ref}/\mathrm{d}V\right)\left[1+g\left(\mathrm{d}^2h_{ref}/\mathrm{d}V^2\right)\right]}{\sqrt{1-\left[\frac{-D(\mathrm{d}h_{ref}/\mathrm{d}V)}{V+g(\mathrm{d}h_{ref}/\mathrm{d}V)}\right]^2}\left[V+g\left(\mathrm{d}h_{ref}/\mathrm{d}V\right)\right]^2} \tag{36}$$

$$\cos\sigma_{ref}=\frac{DV\left(D+g\sin\theta_{ref}\right)\left(\left(\mathrm{d}^2h_{ref}/\mathrm{d}V^2\right)\left(V+g\left(\mathrm{d}h_{ref}/\mathrm{d}V\right)\right)-\left(\mathrm{d}h_{ref}/\mathrm{d}V\right)\left(1+g\left(\mathrm{d}^2h_{ref}/\mathrm{d}V^2\right)\right)\right)}{L\sqrt{1-\left(\frac{-D(\mathrm{d}h_{ref}/\mathrm{d}V)}{V+g(\mathrm{d}h_{ref}/\mathrm{d}V)}\right)^2}\left(V+g\left(\mathrm{d}h_{ref}/\mathrm{d}V\right)\right)^2} -\frac{\left(V^2/r-g\right)\cos\theta_{ref}}{L} \tag{37}$$

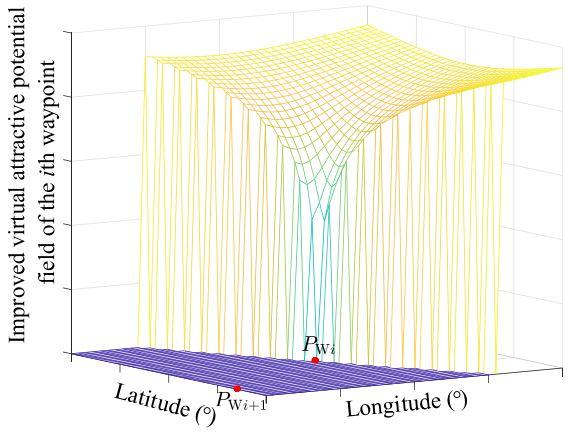

FIGURE 4. The improved virtual attractive potential field of waypoints.

P_{Nj} and P_{Wi}. The improved virtual repulsive potential field of no-fly zones is shown in Fig. 5.

The improved virtual repulsive force of the jth no-fly zone can be expressed as

$$\boldsymbol{F}_{Nj}(P)=\begin{cases}\boldsymbol{F}_{N_1j}(P)+\boldsymbol{F}_{N_2j}(P) & \left(s\left(P,P_{Nj}\right)\geq R_{Nj},\ \angle PP_{NWj}P_{Wi}>\dfrac{\pi}{2}\right)\\ 0 & \left(s\left(P,P_{Nj}\right)\geq R_{Nj},\ \angle PP_{NWj}P_{Wi}\leq\dfrac{\pi}{2}\right)\end{cases}\quad(j=1,2,\ldots,M)\tag{45}$$

where $\boldsymbol{F}_{N_1j}(P)$ is the virtual force attracted by the next waypoint, which effects an approach for the HGV to the next waypoint and is designed as

$$\boldsymbol{F}_{N_1j}(P)=k_N\frac{s(P,P_{Wi})\,s\left(P,P_{Nj}\right)\psi_{Nj}}{\left[s\left(P,P_{Nj}\right)-R_{Nj}\right]^3}\boldsymbol{n}_{N_1j}\tag{46}$$

where $\boldsymbol{n}_{N_1j}=\left(\sin\psi_{N_1j},\cos\psi_{N_1j}\right)^T$ is the unit vector pointing to the next waypoint, whose heading angle ψ_{N_1j} is

$$\psi_{N_1j}=\psi_b(P,P_{Wi})\tag{47}$$

$\boldsymbol{F}_{N_2j}(P)$ is the virtual repulsive force generated by the jth no-fly zone, which is given as follows.

$$\boldsymbol{F}_{N_2j}(P)=\frac{1}{2}k_N\frac{s(P,P_{Wi})^2}{\left[s\left(P,P_{Nj}\right)-R_{Nj}\right]^3}\boldsymbol{n}_{N_2j}\tag{48}$$

where $\boldsymbol{n}_{N_2j}=\left(\sin\psi_{N_2j},\cos\psi_{N_2j}\right)^T$ is the unit vector that is orthogonal to the direction from the HGV to the center of the jth no-fly zone, and the angle between $\boldsymbol{F}_{N_1j}(P)$ and $\boldsymbol{F}_{N_2j}(P)$ is no more than 90°. So the heading angle can be calculated as

$$\psi_{N_2j}=\begin{cases}\psi_b\left(P,P_{Nj}\right)+\dfrac{\pi}{2} & \left(\psi_b\left(P,P_{Nj}\right)\leq\psi_{N_1j}\right)\\ \psi_b\left(P,P_{Nj}\right)-\dfrac{\pi}{2} & \left(\psi_b\left(P,P_{Nj}\right)>\psi_{N_1j}\right)\end{cases}\tag{49}$$

3) THE IMPROVED VIRTUAL REPULSIVE POTENTIAL FIELD OF THREATS

When the great arc distance between the HGV and the center of the threat is less than the detection range R_{det}, the HGV detects the information of the threat and begins maneuvers to avoid it. The threats provide virtual repulsive forces like no-fly zones, and the form of the improved virtual repulsive potential field of threats can be designed as no-fly zones. But because of the limitation on the detection range, threats are much more formidable than no-fly zones. Hence, the improved virtual repulsive potential field of a threat is redesigned as

$$U_{Tk}(P)=\begin{cases}\dfrac{1}{2}k_T\dfrac{s(P,P_{Wi})^2\,s(P,P_{Tk})\,\psi_{Tk}}{s(P,P_{Tk})-R_{Tk}} & \left(R_{Tk}\leq s(P,P_{Tk})<R_{det},\ \angle PP_{TWk}P_{Wi}>\dfrac{\pi}{2}\right)\\ 0 & \left(s(P,P_{Tk})\geq R_{det}\text{ or }\angle PP_{TWk}P_{Wi}\leq\dfrac{\pi}{2}\right)\end{cases}\quad(k=1,2,\ldots,N)\tag{50}$$

where k_T is the repulsive coefficient of threats, $\psi_{Tk}=\angle PP_{Tk}P_{Wi}$ as shown in Fig. 3, P_{Wi} is the next waypoint, and the periphery of the kth threat and the straight line $P_{Tk}P_{Wi}$ are intersected at P_{TWk}. The difference in the improved virtual repulsive potential fields between no-fly zones and threats is the order of the denominator. This leads the improved virtual repulsive forces of threats to be much larger than the other forces, and the HGV can evade threats effectively. The improved virtual repulsive potential field of threats is shown in Fig. 6.

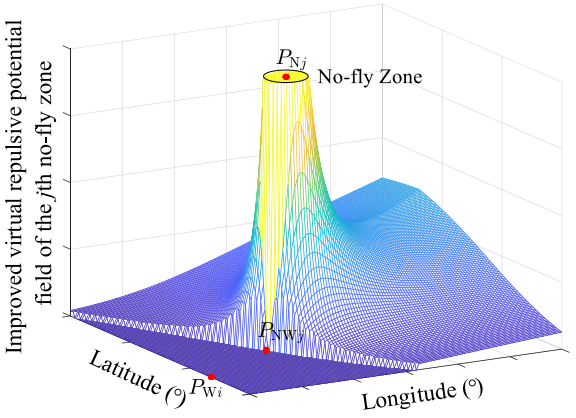

FIGURE 5. The improved virtual repulsive potential field of no-fly zones.

The improved virtual repulsive force of the threat is

$$\boldsymbol{F}_{Tk}(P)=\begin{cases}\boldsymbol{F}_{T_1k}(P)+\boldsymbol{F}_{T_2k}(P) & \left(R_{Tk}\leq s(P,P_{Tk})<R_{det},\ \angle PP_{TWk}P_{Wi}>\dfrac{\pi}{2}\right)\\ 0 & \left(s(P,P_{Tk})\geq R_{det}\text{ or }\angle PP_{TWk}P_{Wi}\leq\dfrac{\pi}{2}\right)\end{cases}\quad(k=1,2,\ldots,N)\tag{51}$$

where $\boldsymbol{F}_{\mathrm{T}_1 k}(P)$ and $\boldsymbol{F}_{\mathrm{T}_2 k}(P)$ are expressed as follows, respectively.

$$\boldsymbol{F}_{\mathrm{T}_1 k}(P) = k_{\mathrm{T}} \frac{s(P, P_{\mathrm{W}i})\, s(P, P_{\mathrm{T}k})\, \psi_{\mathrm{T}k}}{s(P, P_{\mathrm{T}k}) - R_{\mathrm{T}k}} \boldsymbol{n}_{\mathrm{T}_1 k} \tag{52}$$

$$\boldsymbol{F}_{\mathrm{T}_2 k}(P) = \frac{1}{2} k_{\mathrm{T}} \frac{s(P, P_{\mathrm{W}i})^2}{s(P, P_{\mathrm{T}k}) - R_{\mathrm{T}k}} \boldsymbol{n}_{\mathrm{T}_2 k} \tag{53}$$

where $\boldsymbol{F}_{\mathrm{T}_1 k}(P)$ is the virtual attraction force making effects on approaching the next waypoint, $\boldsymbol{n}_{\mathrm{T}_1 k} = \left(\sin \psi_{\mathrm{T}_1 k}, \cos \psi_{\mathrm{T}_1 k}\right)^{\mathrm{T}}$ is the unit vector representing the direction to the next waypoint, whose heading angle $\psi_{\mathrm{T}_1 k}$ is

$$\psi_{\mathrm{T}_1 k} = \psi_b(P, P_{\mathrm{W}i}) \tag{54}$$

$\boldsymbol{F}_{\mathrm{T}_2 k}(P)$ is the virtual repulsive force for avoiding the kth threat, $\boldsymbol{n}_{\mathrm{T}_2 k} = \left(\sin \psi_{\mathrm{T}_2 k}, \cos \psi_{\mathrm{T}_2 k}\right)^{\mathrm{T}}$ is the unit vector that is perpendicular to the direction from the HGV to the center of the kth threat, and the angle between $\boldsymbol{F}_{\mathrm{T}_1 k}(P)$ and $\boldsymbol{F}_{\mathrm{T}_2 k}(P)$ is no more than 90°. So the heading angle can be calculated as

$$\psi_{\mathrm{T}_2 k} = \begin{cases} \psi_b(P, P_{\mathrm{T}k}) + \dfrac{\pi}{2} & \left(\psi_b(P, P_{\mathrm{T}k}) \le \psi_{\mathrm{T}_1 k}\right) \\ \psi_b(P, P_{\mathrm{T}k}) - \dfrac{\pi}{2} & \left(\psi_b(P, P_{\mathrm{T}k}) > \psi_{\mathrm{T}_1 k}\right) \end{cases} \tag{55}$$

B. LATERAL GUIDANCE LAW DESIGN

The magnitude of σ is analytically calculated in Section III, and the sign of σ is determined by the heading corridor to realize the lateral guidance. The reference heading angle is judged by the resultant force extracted from the IAPF method, which is as

$$\psi^* = \angle \boldsymbol{F}_{\mathrm{sum}}(P) \tag{56}$$

where $\angle \boldsymbol{F}_{\mathrm{sum}}(P)$ is the heading angle of the resultant force as demonstrated in Fig. 3, which can be calculated as follows.

$$\boldsymbol{F}_{\mathrm{sum}}(P) = \boldsymbol{F}_{\mathrm{W}i}(P) + \sum_{j=1}^{M} \boldsymbol{F}_{\mathrm{N}j}(P) + \sum_{k=1}^{N} \boldsymbol{F}_{\mathrm{T}k}(P) \tag{57}$$

For guaranteeing the constraint of the ultimate heading error, the heading angle error threshold is defined as

$$\delta\psi = \delta\psi_{\mathrm{f}} \tag{58}$$

So the upper and lower boundaries of the heading corridor are

$$\begin{cases} \psi'_{\mathrm{up}} = \psi^* + \delta\psi \\ \psi'_{\mathrm{down}} = \psi^* - \delta\psi \end{cases} \tag{59}$$

When the HGV approaches a waypoint, the direction of the resultant force is mostly governed by the waypoint, i.e. $\lim_{P \to P_{\mathrm{W}i}} \psi^* = \psi_{\mathrm{W}i}$, resulting in the waypoint being contained inside the heading corridor, as shown in Fig. 7. As the HGV gets closer to the waypoint, the allowable area of the waypoint in Eq. (18) will cover the entire heading corridor, ensuring that the nearest point of the trajectory fits the waypoint constraint. Further for successful circumvention of the no-fly zones and the threats, the heading corridor is reinforced as

$$\begin{cases} \psi_{\mathrm{up}} = \min\left(\psi'_{\mathrm{up}}, \psi^{\mathrm{up}}_{\mathrm{N_T}}, \psi^{\mathrm{up}}_{\mathrm{T_T}}\right) \\ \psi_{\mathrm{down}} = \max\left(\psi'_{\mathrm{down}}, \psi^{\mathrm{down}}_{\mathrm{N_T}}, \psi^{\mathrm{down}}_{\mathrm{T_T}}\right) \end{cases} \tag{60}$$

where $\psi^{\mathrm{up}}_{\mathrm{N_T}}$, $\psi^{\mathrm{down}}_{\mathrm{N_T}}$ are the bearings of the tangent points between the HGV and the no-fly zones, and $\psi^{\mathrm{up}}_{\mathrm{T_T}}$, $\psi^{\mathrm{down}}_{\mathrm{T_T}}$ are the bearings of the tangent points between the HGV and the detected threats, which are illustrated in Fig. 7.

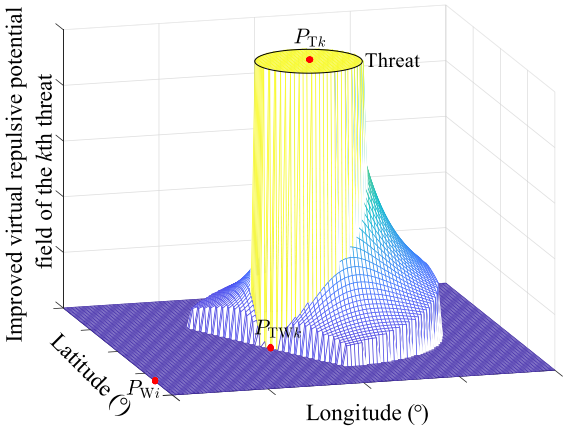

FIGURE 6. The improved virtual repulsive potential field of threats.

Once the HGV glides across the boundary of the heading corridor, the sign of σ is reversed. On the contrary, when the HGV stays in the heading corridor, the sign of σ remains unchanged. So the bank angle logic is designed as follows.

$$\mathrm{sign}(\sigma_{\mathrm{n}}) = \begin{cases} -1 & \left(\psi > \psi_{\mathrm{up}}\right) \\ 1 & \left(\psi < \psi_{\mathrm{down}}\right) \\ \mathrm{sign}(\sigma_{\mathrm{n\text{-}1}}) & \left(\psi_{\mathrm{down}} \le \psi \le \psi_{\mathrm{up}}\right) \end{cases} \tag{61}$$

where σ_{n} is the bank angle at the current time, and $\sigma_{\mathrm{n\text{-}1}}$ is the bank angle of the last guidance command time.

Note that there is a unique scenario when a threat coincides with a waypoint. Because the primary objective of the flight mission is to safely arrive at the terminal coordinate, the threat encountered during the entry process is the most harmful factor that might affect the flight mission. Threat avoidance is more critical than the waypoint pass. If a threat coincides with a waypoint, the HGV will abort passing the waypoint and maneuver to elude the threat. The improved virtual repulsive force of the threat is far greater than the forces generated by the waypoint and the no-fly zones. When the HGV detects a threat, the virtual resultant force is mostly determined by the virtual repulsive force of the threat, and the reference heading angle quickly changes to allow the HGV to avoid the threat. Thus, in the improved virtual potential fields designed in this paper, when the HGV detects a threat that coincides with a

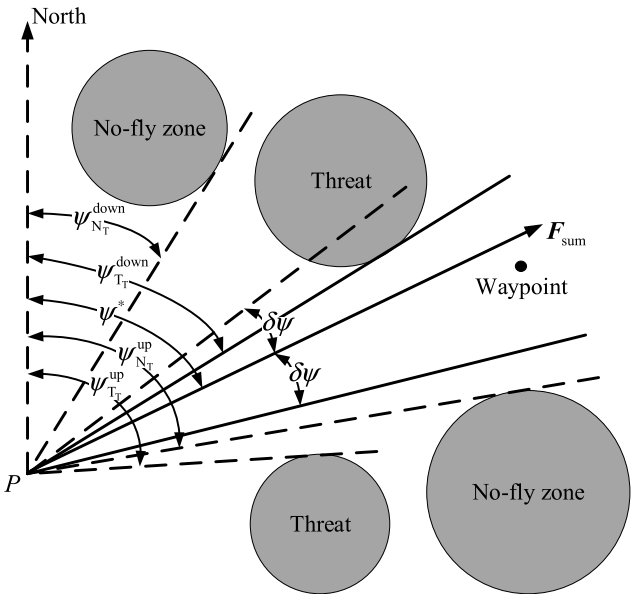

FIGURE 7. The heading corridor.

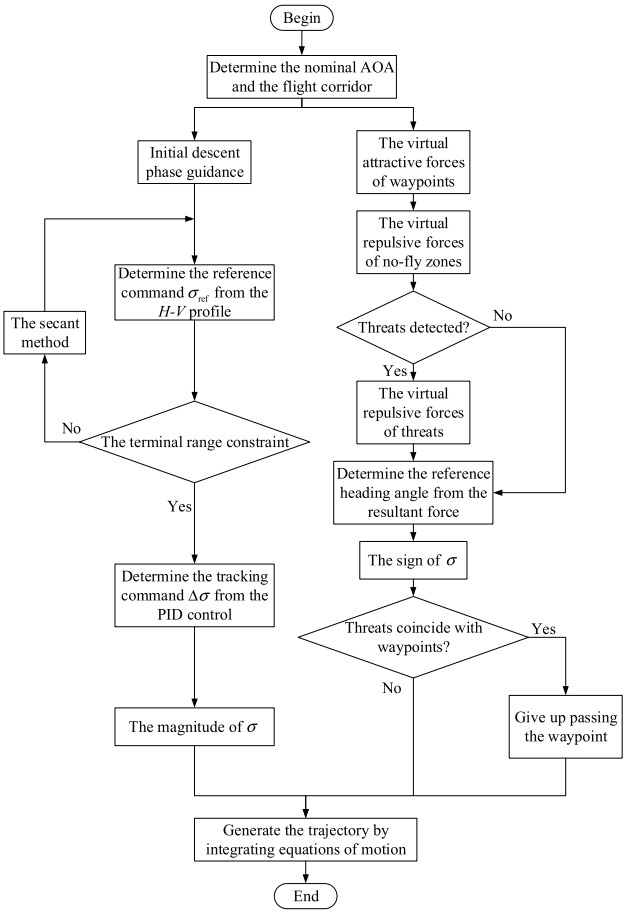

FIGURE 8. The flowchart of the guidance command generation process.

waypoint, the HGV avoids the threat and does not pass the waypoint, ensuring final arrival at the terminal coordinate.

In summary, the process of the guidance command generation is shown in Fig. 8.

TABLE 1. The initial states, the terminal constraints, and the permissible errors.

h_0/km	λ_0/(°)	ϕ_0/(°)	V_0/(m/s)	θ_0/(°)	ψ_0/(°)
80	10	-20	7100	-1	45
h_f^*/km	λ_f^*/(°)	ϕ_f^*/(°)	V_f^*/(m/s)	θ_f^*/(°)	-
25	90	30	2000	-0.5	-
δh_f/km	$\delta\lambda_f$/(°)	$\delta\phi_f$/(°)	δV_f/(m/s)	$\delta\theta_f$/(°)	$\delta\psi_f$/(°)
1	0.5	0.5	100	0.5	8

TABLE 2. The coefficients of the nominal AOA, the tracking guidance, and the IAPF.

α_{max}/(°)	$\alpha_{L/D\,max}$/(°)	k_P	k_I	k_D
20	10	1.5e-4	2e-8	1.5e-4
$V_{\alpha 1}$/(m/s)	$V_{\alpha 2}$/(m/s)	k_W	k_N	k_T
6500	5000	50	5	80

V. NUMERICAL SIMULATIONS AND ANALYSIS

Hereto, the nominal AOA function, the analytical expression of the magnitude of the bank angle, and the bank angle reverse law are determined. Several simulations on the CAV-H model [29] are introduced in this section to confirm the effectiveness of the algorithm. The path constraints are set as $\dot{Q}_{max} = 1000$ kW/m^2, $q_{max} = 200$ kPa, and $n_{max} = 3$. The segment points in the h-V profile are preset as $V_1 = V_f^* + 1000$ and $V_2 = V_{tran} - 400$. The initial states, the terminal constraints, and the permissible errors of all missions are listed in Table 1. The coefficients of the nominal AOA and the IAPF are shown in Table 2. The HGV is capable to detect threats no more than 350km, i.e. $R_{det} = 350$ km.

A. NOMINAL ENTRY MISSIONS

In this section, three nominal entry missions are illustrated without considering aerodynamic parameter uncertainties and initial state deviations. To show the superiority of the EGCG method proposed in this paper, the entry trajectory planning method with dynamic heading angle corridors (ETP-DHC) in Reference [2] and the predictor-corrector guidance algorithm with the APF method (PCG-APF) in Reference [26] are introduced as comparisons. Missions 1 and 2 include waypoints, no-fly zones, and immobile covert threats. Mission 3 simulates the situation that the HGV eludes the hypersonic interceptor as a dynamic threat detected in the entry process. The information of waypoints, no-fly zones, and threats is listed in Table 3. Note that P_{T1} in mission 3 is the initial position of the dynamic threat. To meet the practical applications, the dynamic threat will move to the HGV in accordance with proportional navigation guidance (PNG) after the HGV entries the detection range. The velocity of the dynamic threat is 9 Mach, and the initial heading angle is 30° measured from the north in the clockwise direction. The coefficient of PNG is set as 4, and the maximum available overload of the dynamic threat is 2g.

TABLE 3. Missions with different waypoints, no-fly zones, and threats.

Mission	P_{W1}	$(\varepsilon_\lambda, \varepsilon_\phi)$	P_{N1}	R_{N1}/km	P_{N2}	R_{N2}/km	P_{T1}	R_{T1}/km
1	(65°,15°)	(0.5°,0.5°)	(45°,15°)	300	-	-	(55°,8°)	250
2	(65°,15°)	(0.5°,0.5°)	(40°,15°)	300	(60°,5°)	300	(75°,21°)	150
3	(65°,15°)	(0.5°,0.5°)	(40°,15°)	300	-	-	(50°,8°)	10

TABLE 4. Terminal states and errors with the EGCG method.

Mission	h_f/km	Δh_f/m	(λ_f, ϕ_f)	$\Delta\lambda_f$/(°)	$\Delta\phi_f$/(°)	V_f/(m/s)	ΔV_f/(m/s)	θ_f/(°)	$\Delta\theta_f$/(°)
1	24.8803	119.6805	(89.9832°,30.0111°)	0.0168	0.0111	1999.9468	0.0532	-0.8351	0.3351
2	24.8301	169.9343	(90.0134°,29.9854°)	0.0134	0.0146	1999.9719	0.0281	-0.8244	0.3244
3	24.8752	124.8252	(90.3815°,30.2764°)	0.3815	0.2764	1999.9472	0.0528	-0.8164	0.3164

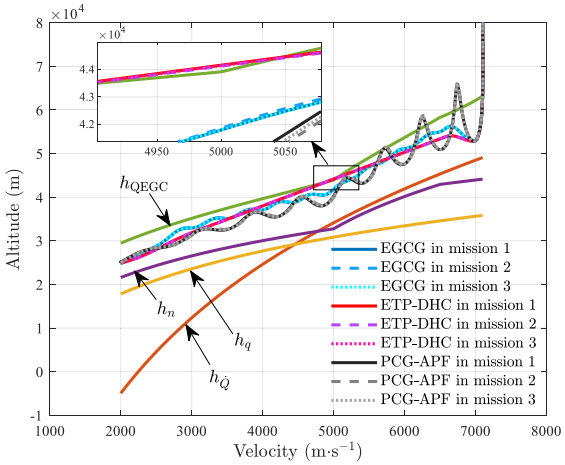

FIGURE 9. *h-V* profiles.

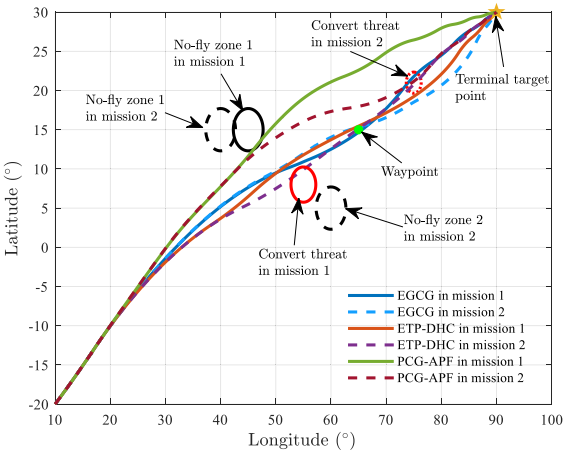

FIGURE 10. The ground trajectories in missions 1 and 2.

The selection of the initial position, the terminal position, waypoints, no-fly zones, and threats of all the flight missions is only considered academically, without any political meanings. Because the trajectory planning method proposed in Reference [2] and the guidance algorithm in Reference [26] don't consider threats, the threats are regarded as no-fly zones in the simulations with the compared methods, which means the information of threats is known before launch with the ETP-DHC and the PCG-APF. The simulation results with threats are shown in Figs. 9-14.

With the EGCG method, the proportionality coefficients k of the h-V profiles in the missions are equal to 0.22399, 0.21626, and 0.21773. The h-V profiles are determined by the ranges and altitudes, so the proportionality coefficients are micro close due to the same terminal constraints of three missions. Fig. 9 gives the h-V profiles, which show that the gliding phase with the EGCG method stabilizes in the entry corridor and the HGV satisfies the path constraints. While the h-V profiles with the ETP-DHC exceed the upper boundary of the entry corridor and violate the QEGC constraint. This is because the middle piece of the h-V profile polynomial designed in Reference [2] is a straight line and the entry corridor is tortuous. When the range requirement of the mission is very large, the HGV needs to fly at a high altitude with a large velocity, which causes the h-V profile to be too close to the upper boundary of the entry corridor and exceed it. On the contrary, the reference h-V profile with the EGCG method is mainly parallel to the boundaries of the entry corridor, which is beneficial to fully use the width of the entry corridor and guarantees the satisfaction of path constraints under a large range requirement. The longitudinal guidance of the PCG-APF doesn't consider the QECG constraint and violates it. As shown in Fig. 9, the h-Vprofiles with the ETP-DHC are very smooth, which is due to the exclusion of the command tracking in the entry trajectory planning process in Reference [2]. The h-V profiles with the EGCG method are much less undulant than the PCG-APF.

The ground trajectories are shown in Fig. 10 and Fig. 11, and the terminal states and errors with the EGCG method are listed in Table 4, which can be indicated that the EGCG method allows the HGV to fly over waypoints, avoid no-fly zones, steer by threats, and accurately reach the terminal target point at the specified altitude, velocity, and flight path angle. Especially in mission 3, the HGV can avoid the

dynamic threat with PNG, as shown in the partially enlarged detail of Fig. 11. The ground trajectory with the ETP-DHC meets the requirements in mission 1. However, in mission 2, even the information of the covert threat is known before launch, the HGV with the ETP-DHC still crosses the covert threat. In mission 3, the dynamic threat hits the HGV at $t = 936$s. The ground trajectories with the PCG-APF don't pass the waypoint in all missions. The HGV with the PCG-APF doesn't avoid the no-fly zone in mission 1 and the threat in mission 2. In mission 3, the distance of the threat from the HGV with the PCG-APF is more than the detection range all the time, so the threat doesn't move to the HGV.

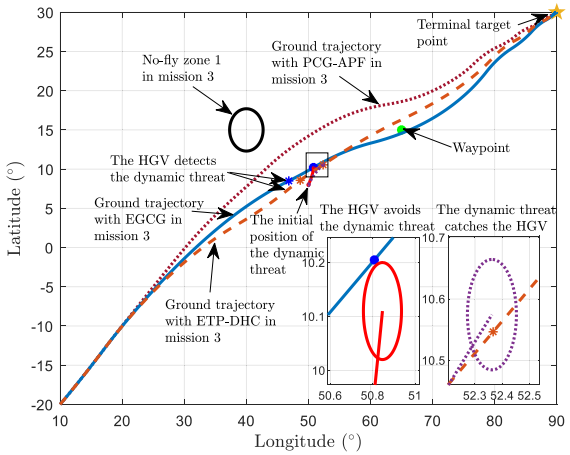

FIGURE 11. The ground trajectories in mission 3.

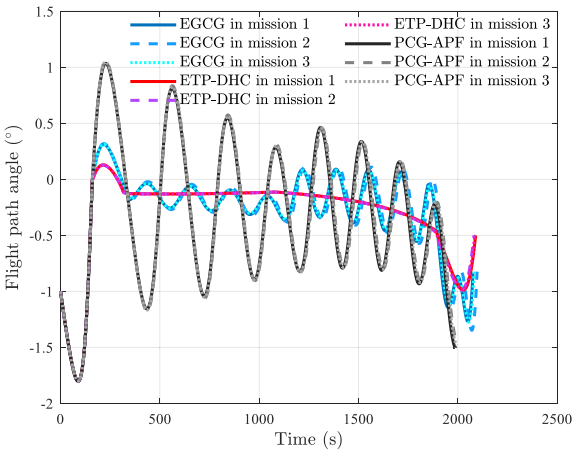

FIGURE 12. Flight path angles.

The flight path angles with the three methods are demonstrated in Fig. 12. The flight path angle is only determined by the longitudinal guidance logic, so the curves of the flight path angle with the same method are very similar. The ETP-DHC is only a trajectory planning method without considering the command tracking, which generates very smooth curves of the flight path angle. The flight path angles with the EGCG method are much less oscillating than the PCG-APF.

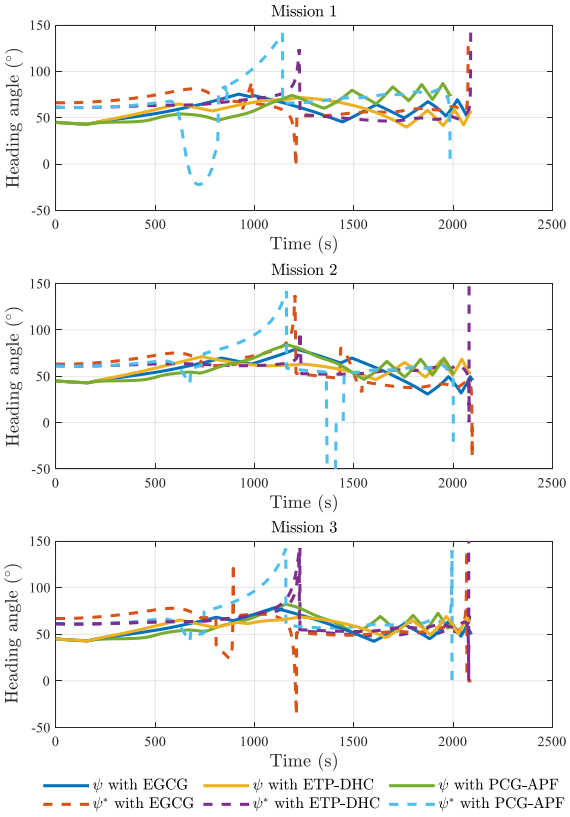

FIGURE 13. Heading angles and references.

Fig. 13 displays the heading angles of the HGV and the reference heading angles in different missions. Fig. 14 illustrates the bank angles of the HGV with three different methods. The reference heading angle with the ETP-DHC is only influenced by the waypoints. So there is only one sudden change in the curve of ψ^* with the ETP-DHC in every mission. Moreover, there are situations of no feasible heading angle corridor satisfying all geographic constraints that happened in the simulations with the ETP-DHC. All these reasons result in the violation of threat constraints in mission 2 with the ETP-DHC. With the EGCG method proposed in this paper and the PCG-APF in Reference [26], the reference heading angle is the same as the direction of the virtual resultant force determined by the waypoints, no-fly zones, and threats, which makes the heading angle corridors with the EGCG method and the PCG-APF exist all the time in different missions. While the attractive potential field and the repulsive potential field in the PCG-APF are both designed as Napierian logarithm forms, the APFs in the EGCG method have different forms according to the characteristics of waypoints, no-fly zones, and threats. Hence, the HGV with the EGCG method possesses a stronger capability than the PCG-APF to pass waypoints, elude no-fly zones, and avoid threats.

In mission 1, ψ^* with the EGCG method suddenly changes at $t = 828.5$s, because the HGV just bypasses the no-fly zone. Then from $t = 925$s to $t = 989$s, the HGV with the EGCG method detects the covert threat, and the bank angle reverses twice to make a detour around the covert threat. The HGV

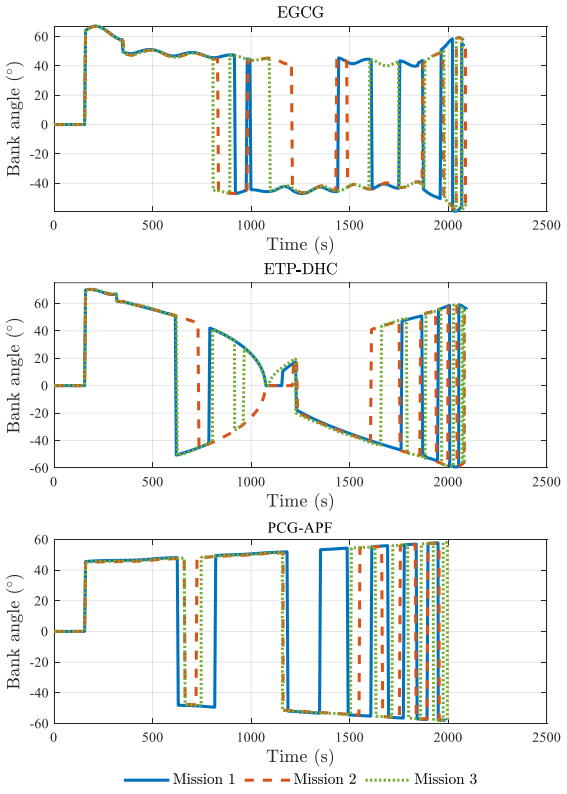

FIGURE 14. Bank angles.

flies over the waypoint at $t = 1214$s, and the HGV veers to the target, so there is a cusp in the curve of ψ^*. In mission 2 with the EGCG method, the HGV bypasses the two no-fly zones at $t = 729$s and $t = 945$s, respectively. The time that the HGV glides across the waypoint is $t = 1206.1$s. The HGV discovers the covert threat at $t = 1426.1$s, and therefore ψ^* occurs an abrupt change so that the bank angle switches to the opposite direction at that time. In mission 3, the HGV with the EGCG method circumvents the no-fly zone at $t = 728.8$s. At $t = 806$s, the HGV detects the incoming dynamic threat and swerves to avoid it. Then at $t = 893.8$s, the HGV successfully avoids the dynamic threat, which is shown in the partially enlarged detail of Fig. 11. The waypoint is passed at $t = 1211.7$s.

B. MONTE CARLO SIMULATIONS

In the entry phase, the uncertainties of the atmospheric environment and the strong disturbances of the HGV's initial states may cause the HGV to deviate from the initial trajectory or the target, and even lead to the failure of the mission. To further evaluate the robustness of the EGCG method proposed in this paper, a dispersion study is executed for Mission 1 by Monte Carlo simulations. The distributions of the initial condition and modeling errors are Gaussian distributed, which are shown in Table 5, where σ is the standard deviation. The simulation results of 1000 dispersed cases are shown in Figs. 15-18.

As shown in Fig. 15, despite the existence of aerodynamic parameter uncertainties and the deviations of initial states,

TABLE 5. Dispersions in monte carlo simulations.

Error	Mean	3σ	Error	Mean	3σ
Δh_0/km	0	1.0	$\Delta\psi_0/(°)$	0	10
$\Delta\lambda_0/(°)$	0	0.1	$\Delta C_L/\%$	0	10
$\Delta\phi_0/(°)$	0	0.1	$\Delta C_D/\%$	0	10
$\Delta V_0/(\mathrm{m/s})$	0	100	$\Delta\rho/\%$	0	5
$\Delta\theta_0/(°)$	0	0.1			

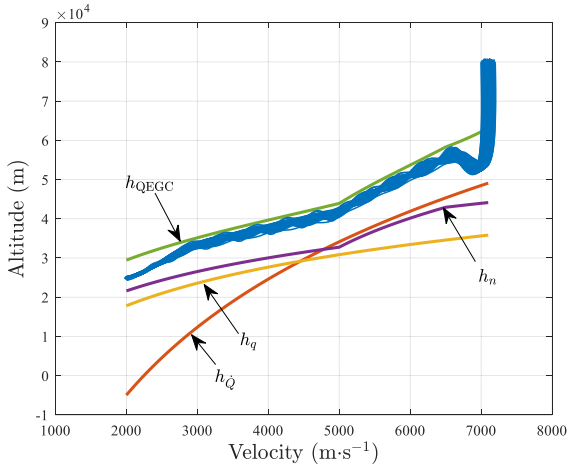

FIGURE 15. *h-V* profiles in monte carlo simulations.

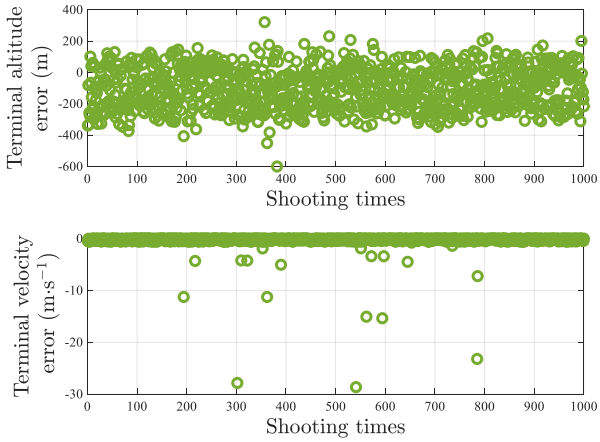

FIGURE 16. Terminal altitude errors and velocity errors in Monte Carlo simulations.

all of the H-V profiles in 1000 dispersed cases are stable in the entry corridor. Fig. 16 demonstrates the terminal altitude errors and velocity errors, which are all in the permissible ranges of terminal altitude and velocity constraints. The maximum and mean terminal altitude errors are -600.054m and -101.9362m, respectively. The maximum and mean terminal velocity errors are -28.6408m/s and -0.3447m/s, respectively. The ground trajectories and the terminal position coordinates in Monte Carlo simulations are displayed in Fig. 17 and Fig. 18, respectively. From Fig. 17, it can be indicated that the EGCG method proposed in this paper

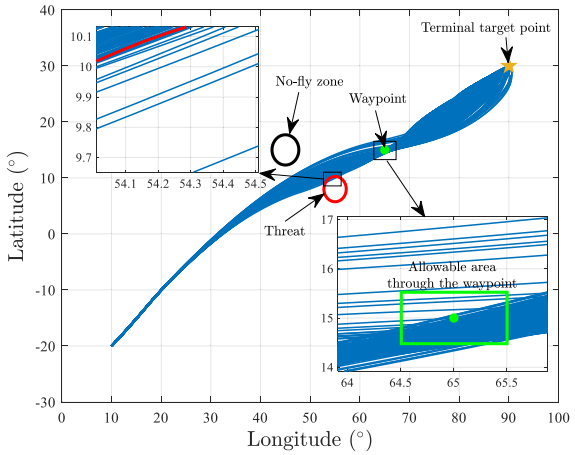

FIGURE 17. The ground trajectories in monte carlo simulations.

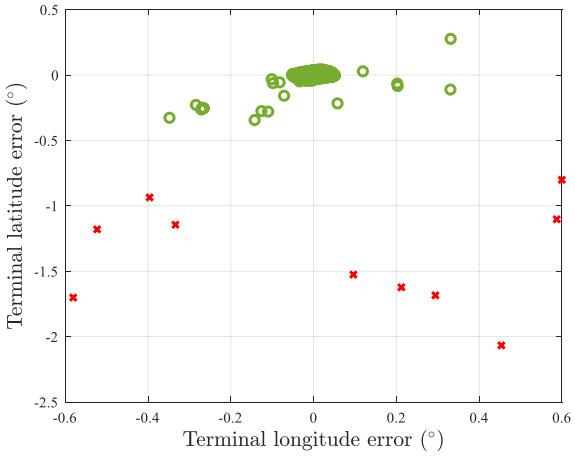

FIGURE 18. Terminal position coordinates in monte carlo simulations.

can successfully guide the HGV to avoid the no-fly zone. But as shown in the partially enlarged details in Fig. 17, the HGVs in 12 dispersed cases enter the hazardous range of the threat and 7 ground trajectories don't pass the waypoint. 10 terminal points, which are depicted as red crosses in Fig. 18, exceed the terminal geographic constraint. The maximum and mean terminal distance errors are 234.05km and 10.67km, respectively. The success rate in Monte Carlo simulations of the EGCG method with atmospheric uncertainties and initial state deviations is 97.1%. The Monte Carlo simulation results show that the proposed EGCG method has high robustness and stability.

VI. CONCLUSION

The EGCG method proposed in this paper is established on the analytical command magnitude calculation and the IAPF method. In addition to typical trajectory constraints, covert threats and dynamic threats are considered in the process of entry. The magnitude of bank angle commands is deduced from the analytical piecewise longitudinal trajectory polynomial in h-V profile and the PID tracking control. The improved virtual potential fields are designed for waypoints, no-fly zones, and threats, respectively. The sign of bank angles is determined by the direction of the resultant forces in the IAPF. Numerical simulations consider fixed and mobile threats, and the results show that the algorithm can provide enormous capacities for accurate target point arrival of the HGV in specific terminal conditions, and strong robustness against aerodynamic uncertainties and initial state deviations. An important outcome of this approach is that even when the existence of threats governs the entry trajectories more complex, the EGCG method possesses excellent abilities to satisfy all kinds of constraints and circumvent every threat.

ACKNOWLEDGMENT

The authors would like to thank the editors and the anonymous reviewers whose insightful comments have helped to improve the quality of this paper considerably.

REFERENCES

[1] W. Zhang, W. Chen, and W. Yu, "Entry guidance for high-L/D hypersonic vehicle based on drag-vs-energy profile," *ISA Trans.*, vol. 83, pp. 176–188, Dec. 2018.
[2] X. Wang, J. Guo, S. Tang, S. Qi, and Z. Wang, "Entry trajectory planning with terminal full states constraints and multiple geographic constraints," *Aerosp. Sci. Technol.*, vol. 84, pp. 620–631, Jan. 2019.
[3] Y. Shi and Z. Wang, "A deep learning-based approach to real-time trajectory optimization for hypersonic vehicles," in *Proc. AIAA Scitech Forum*, Orlando, FL, USA, Jan. 2020, p. 23.
[4] J. Yu, X. Dong, Q. Li, Z. Ren, and J. Lv, "Cooperative guidance strategy for multiple hypersonic gliding vehicles system," *Chin. J. Aeronaut.*, vol. 33, no. 3, pp. 990–1005, Mar. 2020.
[5] P. Lu, "Entry guidance: A unified method," *J. Guid., Control, Dyn.*, vol. 37, no. 3, pp. 713–728, Feb. 2014.
[6] S. B. Xue and P. Lu, "Constrained predictor-corrector entry guidance," *J. Guid., Control, Dyn.*, vol. 33, no. 4, pp. 1273–1281, Jul. 2010.
[7] P. Lu, C. W. Brunner, S. J. Stachowiak, G. F. Mendeck, M. A. Tigges, and C. J. Cerimele, "Verification of a fully numerical entry guidance algorithm," *J. Guid., Control, Dyn.*, vol. 40, no. 2, pp. 230–247, Feb. 2017.
[8] T. Wang, H. Zhang, and G. Tang, "Predictor-corrector entry guidance with waypoint and no-fly zone constraints," *Acta Astronautica*, vol. 138, pp. 10–18, Sep. 2017.
[9] K. Zhang and W. Chen, "Reentry vehicle constrained trajectory optimization," in *Proc. 17th AIAA Int. Space Planes Hypersonic Syst. Technol. Conf.*, San Francisco, CA, USA, Apr. 2011, p. 2231.
[10] J. Zhao and R. Zhou, "Particle swarm optimization applied to hypersonic reentry trajectories," *Chin. J. Aeronaut.*, vol. 28, no. 3, pp. 822–831, Jun. 2015.
[11] H. Y. Zhou, X. Wang, B. Bai, and N. Cui, "Reentry guidance with constrained impact for hypersonic weapon by novel particle swarm optimization," *Aerosp. Sci. Technol.*, vol. 78, pp. 205–213, Jul. 2018.
[12] Y. Wu, J. Yao, and X. Qu, "An adaptive reentry guidance method considering the influence of blackout zone," *Acta Astronautica*, vol. 142, pp. 253–264, Jan. 2018.
[13] R. Chai, A. Tsourdos, A. Savvaris, S. Chai, and Y. Xia, "Trajectory planning for hypersonic reentry vehicle satisfying deterministic and probabilistic constraints," *Acta Astronautica*, vol. 177, pp. 30–38, Dec. 2020.
[14] Z. Wang, "Optimal trajectories and normal load analysis of hypersonic glide vehicles via convex optimization," *Aerosp. Sci. Technol.*, vol. 87, pp. 357–368, Apr. 2019.
[15] J. C. Harpold and C. A. Graves, Jr., "Shuttle entry guidance," presented at the 25th Amer. Astron. Soc., Anniversary Conf., Houston, TX, USA, Oct. 1978.
[16] W. Yu and W. Chen, "Entry guidance with real-time planning of reference based on analytical solutions," *Adv. Space Res.*, vol. 55, no. 9, pp. 2325–2345, May 2015.
[17] L. Yang, J. Yang, W. Chen, and H. Liu, "Entry guidance with no-fly zone avoidance using linear pseudospectral model predictive control," *IEEE Access*, vol. 7, pp. 98589–98602, 2019.

[18] J. Guo, X. Wu, and S. Tang, "Autonomous gliding entry guidance with geographic constraints," *Chin. J. Aeronaut.*, vol. 28, no. 5, pp. 1343–1354, Oct. 2015.
[19] D. Wang, S. Chen, Y. Zhang, and L. Liu, "Path planning of mobile robot in dynamic environment: Fuzzy artificial potential field and extensible neural network," *Artif. Life Robot.*, vol. 26, no. 1, pp. 129–139, Feb. 2021.
[20] Z. Du, D. Zhao, J. Shi, and J. Lu, "Formation flight in complex environments using an artificial potential field," *J. Aerosp. Inf. Syst.*, vol. 18, no. 7, pp. 464–475, Jul. 2021.
[21] C. Yuan, S. Weng, J. Shen, L. Chen, Y. He, and T. Wang, "Research on active collision avoidance algorithm for intelligent vehicle based on improved artificial potential field model," *Int. J. Adv. Robotic Syst.*, vol. 17, no. 3, pp. 1–10, May 2020.
[22] J. Song, C. Hao, and J. Su, "Path planning for unmanned surface vehicle based on predictive artificial potential field," *Int. J. Adv. Robotic Syst.*, vol. 17, no. 2, pp. 1–13, Mar. 2020.
[23] H. Zhou, S. Zhou, J. Yu, Z. Zhang, and Z. Liu, "Trajectory optimization of pickup manipulator in obstacle environment based on improved artificial potential field method," *Appl. Sci.*, vol. 10, no. 3, p. 935, Jan. 2020.
[24] D. Zhang, L. Liu, and Y. Wang, "On-line reentry guidance algorithm with both path and no-fly zone constraints," *Acta Astronautica*, vol. 117, pp. 243–253, Dec. 2015.
[25] Z. Li, X. Yang, X. Sun, G. Liu, and C. Hu, "Improved artificial potential field based lateral entry guidance for waypoints passage and no-fly zones avoidance," *Aerosp. Sci. Technol.*, vol. 86, pp. 119–131, Mar. 2019.
[26] Y. Hu, C. Gao, J. Li, W. Jing, and W. Chen, "A novel adaptive lateral reentry guidance algorithm with complex distributed no-fly zones constraints," *Chin. J. Aeronaut.*, to be published, doi: 10.1016/j.cja.2021.06.016.
[27] K. Zhang, "On-board three-dimensional trajectory planning for reentry vehicle," in *Proc. 20th AIAA Int. Space Planes Hypersonic Syst. Technol. Conf.*, Glasgow, U.K., Jul. 2015, p. 3500.
[28] L. Mu, X. Yu, Y. M. Zhang, P. Li, and X. Wang, "Onboard guidance system design for reusable launch vehicles in the terminal area energy management phase," *Acta Astronautica*, vol. 143, pp. 62–75, Feb. 2018.
[29] T. H. Phillips, "A common aero vehicle (CAV) model, description, and employment guide," Schafer Corporation for AFRL and AFSPC, Arlington, TX, USA, Tech. Rep., Jan. 2003.
[30] R. Chai, A. Tsourdos, A. Savvaris, Y. Xia, and S. Chai, "Real-time reentry trajectory planning of hypersonic vehicles: A two-step strategy incorporating fuzzy multiobjective transcription and deep neural network," *IEEE Trans. Ind. Electron.*, vol. 67, no. 8, pp. 6904–6915, Aug. 2020.
[31] L. D. Fairfax, J. D. Vasile, L. Strohm, and F. Fresconi, "Trajectory shaping for quasi-equilibrium glide in guided munitions," in *Proc. AIAA Scitech Forum*, Orlando, FL, USA, Jan. 2020, p. 21.
[32] B. Lin, M. Carpenter, and O. de Weck, "Simultaneous vehicle and trajectory design using convex optimization," in *Proc. AIAA Scitech Forum*, Orlando, FL, USA, Jan. 2020, p. 160.
[33] M. Vedantam, M. R. Akella, and M. J. Grant, "Multi-stage stabilized continuation for indirect optimal control of hypersonic trajectories," in *Proc. AIAA Scitech Forum*, Orlando, FL, USA, Jan. 2020, p. 472.

ZIYAO WANG received the B.S. degree from the Beijing Institute of Technology, in 2016, where he is currently pursuing the Ph.D. degree with the Key Laboratory of Dynamics and Control of Flight Vehicle, School of Aerospace Engineering. His research interests include guidance and control of flight vehicles.

SHENGJING TANG received the B.S. and M.S. degrees from the Beijing Institute of Technology, in 1982 and 1987, respectively, and the Ph.D. degree from the Technical University of Munich, in 2002. He is currently a Professor and the Ph.D. Supervisor with the Key Laboratory of Dynamics and Control of Flight Vehicle, School of Aerospace Engineering, Beijing Institute of Technology. His research interests include dynamics and control of flight vehicles and aircraft overall design.

JIE GUO received the B.S., M.S., and Ph.D. degrees from the Beijing Institute of Technology, in 2004, 2006, and 2010, respectively. He is currently an Associate Professor with the Key Laboratory of Dynamics and Control of Flight Vehicle, School of Aerospace Engineering, Beijing Institute of Technology. His research interests include guidance and control of flight vehicles and aircraft overall design.